Precipitation Estimates from SMOS Sea-Surface Salinity

Alexandre Supply, Jacqueline Boutin, Jean-Luc Vergely, Nicolas Martin, Audrey Hasson, Gilles Reverdin, Cécile Mallet, Nicolas Viltard

▶ **To cite this version:**

Alexandre Supply, Jacqueline Boutin, Jean-Luc Vergely, Nicolas Martin, Audrey Hasson, et al.. Precipitation Estimates from SMOS Sea-Surface Salinity. Quarterly Journal of the Royal Meteorological Society, 2018, 144 (S1), pp.103-119. ⟨10.1002/qj.3110⟩. ⟨insu-01563248⟩

HAL Id: insu-01563248

https://insu.hal.science/insu-01563248v1

Submitted on 22 Dec 2020

HAL is a multi-disciplinary open access archive for the deposit and dissemination of scientific research documents, whether they are published or not. The documents may come from teaching and research institutions in France or abroad, or from public or private research centers.

L'archive ouverte pluridisciplinaire **HAL**, est destinée au dépôt et à la diffusion de documents scientifiques de niveau recherche, publiés ou non, émanant des établissements d'enseignement et de recherche français ou étrangers, des laboratoires publics ou privés.

HAL Authorization

Received: 28 April 2017 | Revised: 16 June 2017 | Accepted: 26 June 2017 | Published on: 7 August 2017

DOI: 10.1002/qj.3110

Quarterly Journal of the Royal Meteorological Society RMetS

Precipitation Estimates from SMOS Sea-Surface Salinity

A. Supply[1] | J. Boutin[1] | J.-L. Vergely[2] | N. Martin[1,†] | A. Hasson[1] | G. Reverdin[1] | C. Mallet[3] | N. Viltard[3]

[1]LOCEAN-IPSL, Sorbonne Universités (UPMC, Univ. Paris 06) - CNRS - IRD – MNHN, Paris, France
[2]ACRI-st, Guyancourt, France
[3]LATMOS-IPSL, Université de Versailles Saint-Quentin-en-Yvelines, Versaille and Université Paris 06, CNRS-INSU, Guyancourt, France

Correspondence
A. Supply, Laboratoire d'Océanographie et du Climat par Expérimentation et Approches Numériques, Institut Pierre Simon Laplace, Unité mixte de Recherche, CNRS/IRD/UPMC/MNHN, Université Pierre et Marie Curie, 4 place Jussieu, 75252 Paris CEDEX 05, France.
Email: alexandre.supply@locean.upmc.fr

Funding information
European Space Agency, STSE SMOS+RAINFALL. Centre National d'Etudes Spatiales, SMOS Ocean/TOSCA.

Two L-Band (1.4 GHz) microwave radiometer missions, Soil Moisture and Ocean Salinity (SMOS) and Soil Moisture Active and Passive (SMAP) currently provide sea-surface salinity (SSS) measurements. At this frequency, salinity is measured in the first centimetre below the sea surface, which makes it very sensitive to the presence of fresh water lenses linked to rain events. A relationship between salinity anomaly (ΔS) and rain rate (RR) is derived in the Pacific intertropical convergence zone from SMOS SSS measurements and Special Sensor Microwave Imager/Sounder (SSMIS) RR. It is then used to develop an algorithm to estimate RR from SMOS SSS measurements. A heuristic function is developed to correct the SMOS-estimated negative RR due to measurement noise. Correlation between SMOS and SSMIS RR and between SMOS and Integrated MultisatellitE Retrievals for GPM (IMERG) RR are high when SMOS and SSMIS passes are less than 15 min apart ($r = 0.7$ at $1° \times 1°$ resolution), showing a good quality of SMOS RR retrievals. When the time shift between SMOS and SSMIS passes increases, the correlation between SMOS and IMERG RR diminishes. This suggests that L-band radiometry can provide information complementary to GPM missions to improve RR products interpolated at high temporal resolution. The retrieval is successfully tested on SMAP SSS. We also check that our algorithm provides reliable estimates of RR when averaged at a monthly time-scale.

KEYWORDS
IMERG, ITCZ, L-band radiometry, precipitation, sea-surface salinity anomalies, SMAP, SMOS

1 | INTRODUCTION

L-band radiometer measurements of salinity provide a synoptic view of the global ocean every 3–7 days. At the present time, three satellite missions carrying L-band radiometers have monitored and/or monitor sea-surface salinity (SSS) from space: Soil Moisture and Ocean Salinity (SMOS) since 2010, Aquarius (between 2011 and 2015) and Soil Moisture Active and Passive (SMAP) since 2015. Over the global ocean, they sense the salinity in the upper first centimetres while most *in situ* measurements are performed at a few metres depth (Boutin et al., 2016) and while current ocean general circulation models usually do not include a description within the upper metre depth. In regions where rain is infrequent, stratification between the first centimetre and a few metres is expected to be small (Henocq et al., 2010). However, in rainy regions, rain leads to the formation of freshwater lenses at the ocean surface and of large vertical salinity gradients. Hence, the interpretation of satellite SSS in rainy regions requires a good knowledge of the rain rate (RR) at the time of the satellite pass. This is often not well informed by meteorological models which do not provide sufficient temporal resolution given the high intermittency of rainfall events and the rapid relaxation of the salinity freshening after a rain event. Actually, in most observational case-studies, salinity anomalies have a short lifetime (typically a few

†Deceased.

 © 2017 Royal Meteorological Society

hours) after a rain event (Drushka, Asher, Ward, & Walesby, 2016; Reverdin, Morisset, Boutin, & Martin, 2012; Soloviev, Lukas, & Matsuura, 2002; Wijesekera, Paulson, & Huyer, 1999), even though some fresh lenses have been observed with a persistence time longer than 15 hr (Walesby, Vialard, Minnett, Callaghan, & Ward, 2015). An alternative is to use merged infrared and passive microwave (PMW) satellite rain products (e.g. CMORPH, IMERG (Integrated MultisatellitE Retrievals for Global Precipitation Measurement)) that provide RR every half-hour (Santos-Garcia et al., 2014) but, as we will show, for cases when there is a time shift of more than 1 hr between the PMW satellite and SMOS, the morphed RR may be imprecise. In this article, we investigate to what extent it is possible to infer RR from L-band radiometric data themselves. Actually, earlier studies (see a review in Boutin et al. (2016)) have shown a strong correlation between the freshening observed by L-band radiometry and RR, at very short time-scale (on the order of half an hour). The observed linear relationships between freshening and RR have a similar order of magnitude to the one predicted by the surface renewal model of the molecular skin layer developed by Schlussel, Soloviev, and Emery (1997). In fact, the thickness of the molecular diffusion layer for salinity is only 0.05 mm but rain induces mixing in the first centimetres of the surface ocean (Ho, Asher, Schlosser, Bliven, & Gordon, 2000; Zappa et al., 2009). The parameters that govern creation and spatial and temporal evolution of these lenses (air–sea fluxes of heat and momentum, upper-ocean mixing, advection) are at present not well understood. Drushka et al. (2016) and Bellenger et al. (2016) have used one-dimensional water column models, the Generalized Ocean Turbulence Model (GOTM) and a prognostic model respectively, to simulate the formation and life cycle of rain-induced fresh lenses. However, given the difficulty of accessing the forcing parameters (e.g. European Centre for Medium-range Weather Forecasts (ECMWF) wind speed is of poor quality in rainy conditions (Portabella et al., 2012)) and given that rain-induced freshening is observed on satellite salinity for ECMWF wind speed between 3 and 12 m/s, we neglect the potential effect of the wind on freshening highlighted by several studies based on *in situ* measurements and modelling (Asher, Jessup, Branch, & Clark, 2014; Bellenger et al., 2016; Drushka et al., 2016). Hence, we will use an empirical relationship between instantaneous freshening and RR observed at moderate wind speed (3–12 m/s) as shown in Boutin et al. (2014). The retrieval algorithm is named PEALS for Precipitations Estimates And L-band Salinity.

In addition to providing important information for users of SMOS SSS, the PEALS-retrieved RR could also complement measurements by PMW radiometers of the Global Precipitation Measurement (GPM) constellation dedicated to rain retrieval and used in merged satellite rain products.

Since the Tropical Rainfall Measuring Mission (TRMM) launch in 1997, a very important breakthrough (Stephens & Kummerow, 2007) was accomplished in retrieving rain from satellite data.

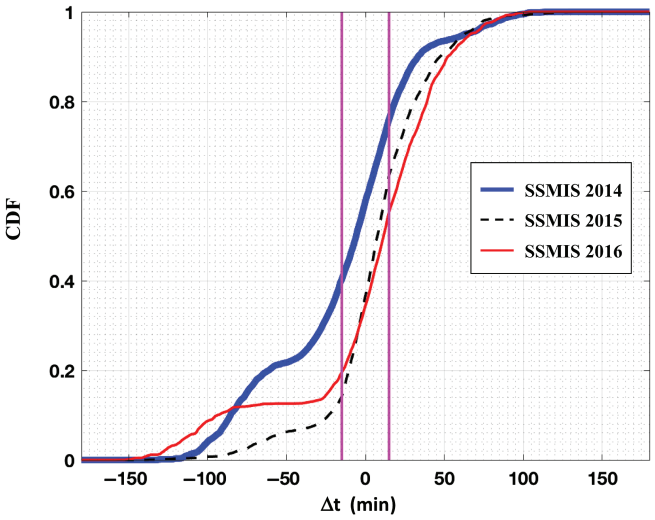

FIGURE 1 Cumulative density function of the temporal shift between SMOS and nearest SSMIS satellite for different years when SSMIS satellite is the nearest PMW satellite from SMOS (time SSMIS − time SMOS). Magenta vertical lines = −15 and +15 min temporal shifts

TRMM was such a successful mission that it was a determining argument to start the GPM project (Hou et al., 2014). This project relies on a Core Observatory similar to TRMM but differing in coverage which extends from 65°S to 65°N and the addition of a Ka-band radar to complement the Ku-band radar. The GPM mother satellite was launched in spring 2014. In addition to the Core Observatory, GPM is also a consortium of space agencies who agreed to share all the data arising from PMW radiometers dedicated to rain retrieval in order to provide users with a rain-oriented dataset giving the best possible coverage (Kidd & Huffman, 2011).

Our study focusses on the retrieval of RR from L-band SSS in the intertropical convergence zone (ITCZ) region (between 180° and 110°W, 0° and 15°N), a region characterized by tropical convective systems for which the spatial resolution of L-band radiometers (~50 km) is well suited (Houze, 2004; Waliser & Gautier, 1993). The chosen region is far from coasts and not affected by freshwater water influx from rivers. The study covers the period from August 2014 to July 2016. The year 2015 corresponds to the training phase. During this year, the Pacific ITCZ was impacted by a rate of precipitation higher than expected, due to El Niño conditions (Bell, Halpert, & L'Heureux, 2016). The other years (2014 and 2016) are used as the validation period. We use SMOS and SMAP data for salinity measurements and the IMERG product for RR.

In Section 2, we present measurements and methods used in this study to estimate salinity anomalies and to relate them to RR. The algorithm developed for deriving RR from satellite salinity, its validation and performance with respect to the RR interpolated product are described in Section 3. Application of the PEALS algorithm to SMAP data is described in Section

4. Finally, results and perspectives of this study are discussed in Section 5.

2 | DATA AND METHODS

The shortest time shift between SMOS SSS and PMW RR is observed in 2015 (Figure 1). So 2015 datasets are used to develop the algorithm for retrieving SMOS RR from satellite salinity, which will be described in Section 3. Validation is done on instantaneous retrievals in 2014 and 2016. Then instantaneous estimates and monthly averages of retrieved SMOS RR are compared with the interpolated RR (IMERG product) during the whole study period.

2.1 | Data description

2.1.1 | Salinity data

SMOS salinity data

SMOS is the first satellite mission that carries an L-band microwave radiometer from which SSS can be retrieved. It was launched in November 2009, and since 2010 provides SSS from space (Kerr et al., 2010). It crosses the Equator at about 6:00 a.m. (0600 hr local time) on ascending node and 6:00 p.m. (1800 hr) in descending node along a Sun-synchronous orbit. The spatial resolution of individual SMOS SSS is close to 50 km. SMOS SSS are oversampled over an Icosahedral Snyder Equal Area (ISEA) grid at 15 km resolution. In the ITCZ, typical noise on individual SMOS SSS is 0.5 pss (practical salinity scale) (Boutin et al., 2014). When averaged over typically 1 month and 100 km × 100 km, the precision of SMOS SSS in tropical regions is improved to typically 0.2–0.3 pss (Boutin, Martin, Reverdin, Yin, & Gaillard, 2013; Hasson, Delcroix, Boutin, Dussin, & Ballabrera-Poy, 2014). Hence, SMOS has already demonstrated its usefulness to investigate different scales of SSS variability (Boutin et al., 2016), but also to detect rain imprint with individual measurements (Boutin et al., 2013, 2014). In this study, we use SMOS level 2 Sea Surface Salinity, S_{sat}, from the second European Space Agency (ESA) reprocessing (v622, Algorithm Theoretical Basis Document available on https://smos.argans.co.uk/docs/deliverables/delivered/ATBD/SO-TN-ARG-GS-0007_L2OS-ATBD_v3.11_140905.pdf) and available on the ESA SMOS Online Dissemination website. Only ascending orbits are considered and in order to avoid uncertainties, we use the same flags as in Boutin et al. (2014).

SMOS S_{sat} are considered only if at least 130 measurements come from the alias-free field-of-view region to ensure a good precision on the retrieved SSS (roughly corresponding to S_{sat} retrieved at 300 km from the centre of the track) and if the associated ECMWF wind speed is between 3 and 12 m/s, in order to avoid uncertain retrievals at very low and high wind speeds.

SMAP salinity data

SMAP was launched in January 2015 into a Sun-synchronous orbit. It uses a single radiometer with a 6 m diameter reflector that allows the retrieval of SSS over the ocean at a 40 km resolution. SMAP was also equipped with an L-Band radar which failed in July 2015. It crosses the Equator at the same time as SMOS but in the opposite phase, near 6:00 a.m. for descending orbits and near 6:00 p.m. for ascending orbits, providing numerous collocations between the two satellites. SMAP SSS data are available since April 2015 to date providing a shared period of more than a year between SMOS and SMAP.

We use SMAP L2B v3.0 data from Jet Propulsion Laboratory (JPL) OurOcean Portal (SMAP Salinity and Wind Speed, Data User's Guide). SMAP L2B SSS are provided by the SMAP TB-only salinity processing, on a grid sampled at about 25 km. Their resolution is 40 km. We use SSS data with valid flags for the quality of data, nominal angles and with all four looks available. At the global scale the root-mean-square difference (RMSD) between individual SMAP SSS and HYCOM SSS is equal to 0.78 pss. The comparison with Argo buoy measurements at 1° × 1° resolution averaged monthly show a standard deviation of 0.2 pss (Fore, Yueh, Tang, Stiles, & Hayashi, 2016).

In this preliminary study, we compare SMOS and SMAP measurements from January 2016 to July 2016. In approximatively 60% of the cases temporal shift between SMOS and SMAP is less than 15 min (less than 30 min in 90% of the cases). In this article, SMAP descending passes are collocated within 15 min of the SMOS ascending passes.

2.1.2 | Rain data

In our study, we consider PMW RR (derived from the Goddard Profiling algorithm (GPROF) scheme), IR RR (derived from Precipitation Estimation from Remotely Sensed Information using Artificial Neural Networks-Cloud Classification System (PERSIANN-CCS)) and interpolated RR (based on morphing techniques) available in IMERG version 03 products (final run (Huffman, 2015a) in 2014 and 2015 and late run (Huffman, 2015b) in 2016) distributed by the Precipitation Processing System at the NASA Goddard Space Flight Center. Precipitation Radar data are not used in this study as the more frequent PMW RR have already been calibrated with respect to Precipitation Radar and have a spatial resolution closer to the one of SMOS measurements. Different RRs provided by the IMERG product are available with a spatial resolution of 0.1° × 0.1°.

Passive microwave rain data

The Global Precipitation Measurement (GPM) mission constellation (Hou et al., 2014) has been designed to provide measured RR using microwave radiometers at least every 3 h. PMW measurements calibration is based on the GPM Core Observatory with the GPM Microwave Imager (GMI)

and the Dual-frequency Precipitation Radar (DPR) (Huffman, Bolvin, & Nelkin, 2015). PMW RR measurement is linked to three physical processes: variability of rain intensities in the radiometer footprint or 'beamfilling effect', the raindrops' size distribution and the effective layer thickness (Hilburn & Wentz, 2008). Different methodologies have been developed to estimate RR from PMW measurements. The Goddard Profiling scheme (GPROF: Kummerow, Olson, & Giglio, 1996) extracts rain information, based on a Bayesian approach and cloud-resolving models, contrary to the Unified Microwave Ocean Retrieval algorithm (UMORA: Hilburn & Wentz, 2008) that is based on a radiative transfer model and an empirical relationship between cloud water liquid path, RR and rain column height. The main differences between these two different algorithms are different microphysical assumptions, cloud and rain partitioning and rain column height (Hilburn & Wentz, 2008). With temporal and spatial smoothing, GPROF and UMORA rain estimates agree very well, but comparisons of individual pixels often indicate very different results (Hilburn & Wentz, 2008). PMW rain products encounter some biases that are compensated by changing the algorithm assumptions as a function of region and time. Further work is needed to characterize the bias as a function of microphysical parameters (Berg, L'Ecuyer, & Kummerow, 2006).

In this article, RR from PMW sensors on board polar-orbiting satellites (R_{PMW}) are derived from the GPROF2014 algorithm and come from a large set of polar-orbiting satellites, such as conical-scan radiometers (Special Sensor Microwave Imager/Sounder (SSMIS), etc.), but also cross-track scanner (Microwave Humidity Sounders (MHS)).

Infrared rain data

IR measurements from the constellation of geostationary satellites provide RR at higher temporal resolution than PMW measurements, with global IR coverage every half hour. IR rain measurements are based on the main assumption that the precipitation intensity is inversely proportional to the cloud-top temperature. While this assumption is valid with time and spatial smoothing, the uncertainty on individual measurements is much higher than the one of PWM rain measurements (Arkin & Meisner, 1987).

Individual satellite RR derived from infrared sensors on board geostationary satellites (R_{IR}) are computed with the PERSIANN-CSS algorithm (Hong, Gochis, Cheng, Hsu, & Sorooshian, 2007) and provided every half-hour. The PERSIANN algorithm uses the higher quality of PMW data for adjusting IR rain information and thus obtains precipitation estimates with higher temporal coverage than with PMW (Sorooshian et al., 2000).

Integrated multisatellite rain estimates

We use the IMERG interpolated rain product. It combines GPM RR from polar-orbiting low frequency PMW with IR

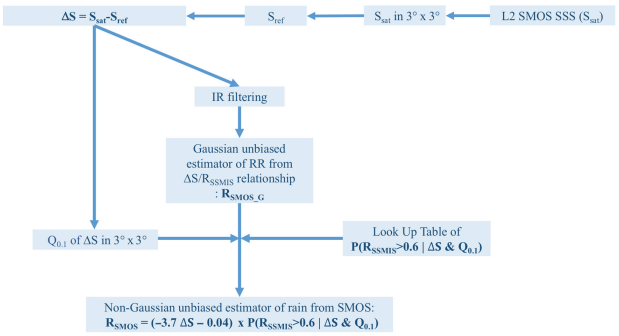

FIGURE 2 Global PEALS algorithm diagram [Colour figure can be viewed at wileyonlinelibrary.com].

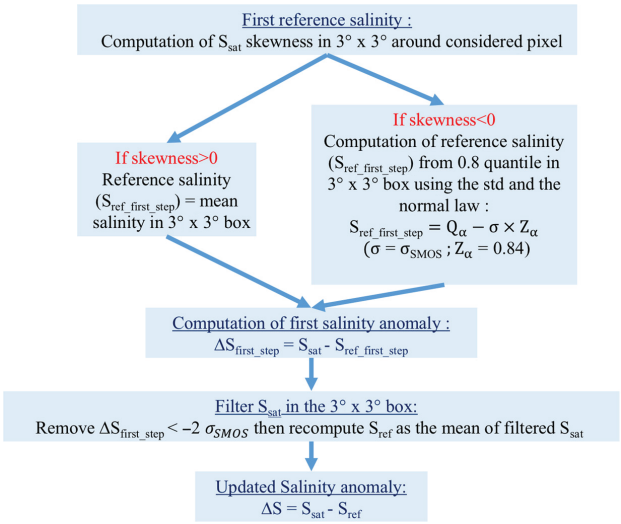

FIGURE 3 Sea-surface salinity anomalies (ΔS) computation process in PEALS algorithm

RR in order to provide RR estimates every 30 min using the morphing technique from the Climate Prediction Center Morphing method (CMORPH: Joyce, Janowiak, Arkin, & Xie, 2004). It takes advantage of the high repetition of IR satellites to monitor the displacement of the rain cells and of the less frequent but more precise R_{PMW}. However, the accuracy of RR derived with morphing method decreases when time shift between considered time and PMW overpass increases (Joyce et al., 2004). Complete IMERG RR fields (R_{IMERG}) are available every 30 min.

2.2 | Methods

The signature of rain on the satellite SSS is a strong decrease of SSS. We quantify this decrease by defining a salinity anomaly with respect to a reference salinity. Once the salinity anomaly is defined, it is collocated with rain products. The PEALS algorithm is fully described in Figure 2.

2.2.1 | Salinity anomalies

The method for deriving salinity anomalies is described below and summarized in Figure 3. The salinity anomaly, ΔS, is defined as the salinity measurement from SMOS, S_{sat},

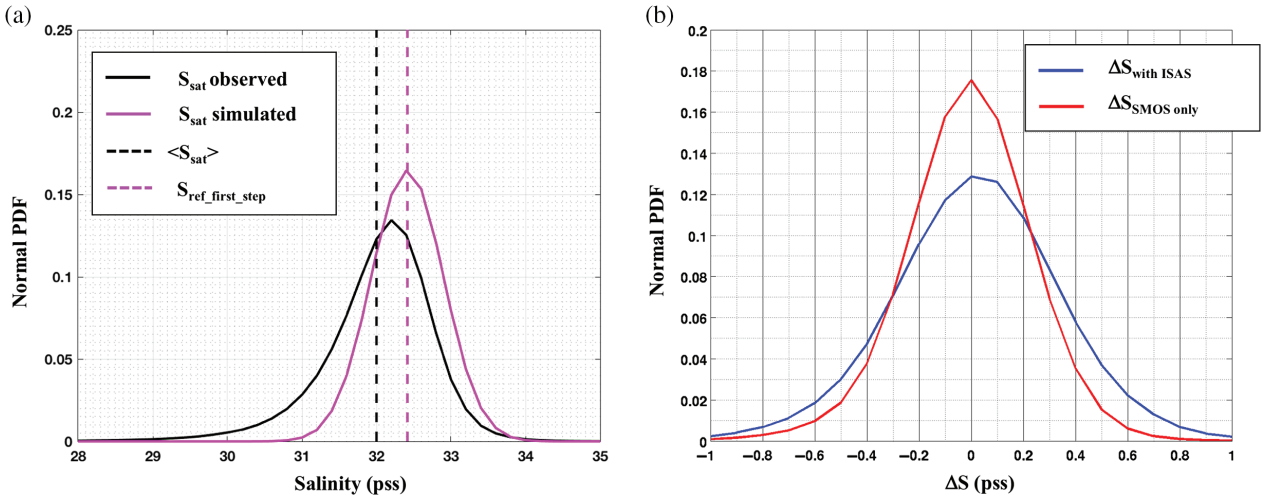

FIGURE 4 (a) $S_{ref\_first\_step}$ computation: (black) example of distribution of salinity observed with SMOS in 3° × 3° area; (magenta) simulated distribution of salinity without rain; black-dashed line: average of salinity observed with SMOS in 3° × 3° area; magenta-dashed line: average simulated salinity without rain = $S_{ref\_first\_step}$. (b) Statistical distribution of ΔS (with 1° × 1° smoothing) computed with the dataset used in Boutin et al. (2014) and only for pixels without rain: (blue) S_{ref} is derived from monthly Argo interpolated field; (red) S_{ref} is derived from SMOS data only following the method used in this article

minus a reference salinity, S_{ref}, not affected by the rain (i.e. corresponding to S_{sat} before the rain event):

$$\Delta S = S_{sat} - S_{ref} \quad (1)$$

S_{ref} computation is derived from the statistical distribution of S_{sat} in a 3° × 3° region. This size is chosen because we observe that such regions are never fully covered by rain, the latitudinal extent of rainy areas being always less than 3°. Hence the statistical distribution of S_{sat} in 3° × 3° always contains information coming from non-rainy pixels. The freshening associated with rain creates in most cases a S_{sat} distribution skewed towards low S_{sat} values (Boutin et al., 2013). The mean of the non-rainy salinities is used for estimating the reference salinity assuming that (a) the upper part of the statistical distribution is affected only by non-rainy salinities, (b) the non-rainy salinities in the 3° × 3° region have a Gaussian distribution due to the noise on SMOS S_{sat}, and (c) the natural variability of the salinity in a 3° × 3° region is negligible in front of SMOS S_{sat} noise. We use an iterative method: in a first step, we estimate the salinity mean, $S_{ref\_first\_step}$, that would be Gaussian distributed and would have the same 0.8 quantile as the observed 3° × 3° distribution:

$$S_{ref\_first\_step} = Q_\alpha - \sigma_{SMOS} \times Z_\alpha. \quad (2)$$

Q_α is the 0.8 quantile of the S_{sat} distribution, σ_{SMOS} is the theoretical error on S_{sat} and Z_α (=0.84) is the theoretical value for the 0.8 quantile for a Gaussian distribution. Figure 4a illustrates the distribution of a 3° × 3° area affected by rain which has a negative skewness and the salinity distribution without rain we simulate from the 0.8 quantile. Nevertheless, the rainy pixels in the observed distribution can make its 0.8 quantile deviate significantly from the 0.8 quantile of a non-rainy Gaussian distribution. This effect is particularly important in the case that a large part of the 3° × 3° area (typically one half) is affected by rain. For this reason we apply a second step in which we first filter the pixels likely to be affected by rain using $S_{ref\_first\_step}$. We remove pixels where (S_{sat} − $S_{ref\_first\_step}$) is less than $-2\sigma_{SMOS}$ and we recompute S_{ref} as the mean salinity in 3° × 3° areas.

The advantages of this approach with respect to using S_{ref} derived from Argo SSS as was done in Boutin et al. (2014) are that (a) it does not use external information for rain determination, hence avoiding errors due to temporal shift between the two measurements, and (b) it will remove any SMOS systematic error with a spatial coherence (e.g. coming from SMOS calibration or from large-scale bias of wind speed (Yin et al., 2014)). This methodology has been applied to the dataset used in Boutin et al. ΔS have a distribution better centred around 0 and with a lower noise than the one obtained using a reference salinity equal to Argo monthly interpolated fields (ISAS: Gaillard et al., 2009) (noise decreases from 0.34 to 0.25 pss; Figure 4b). Three examples of ΔS computed with S_{ref} are shown in Figure 5 with rain isolines; the ΔS pattern seems to qualitatively match with R_{PMW} isolines. Since negative ΔS are sometimes related to other processes than rain freshening, as for instance mesoscale variability or disturbances by radiofrequency interference, we identify pixels close to rainy regions using R_{IR}. Actually, there is always an IR measurement less than 15 min from an SMOS pass. By looking at the spatial distribution of R_{SSMIS} and R_{IR} taken at less than 15 min apart, we find that very few SSMIS rainy pixels occur in 3° × 3° areas where at least one R_{IR} is larger than 0 mm/hr: only 3% of R_{SSMIS} are strictly positive and only 0.2% of R_{SSMIS} are higher than 1 mm/hr (for the training year, 2015). Hence, only SMOS pixels surrounding a R_{IR} larger than 0 mm/hr in 3° × 3° area are considered hereafter to estimate RR.

2.2.2 | Collocations

To ease the spatial collocations, the various gridded products are projected onto a grid regularly sampled in latitude and longitude at 0.2° resolution. The projected values are obtained

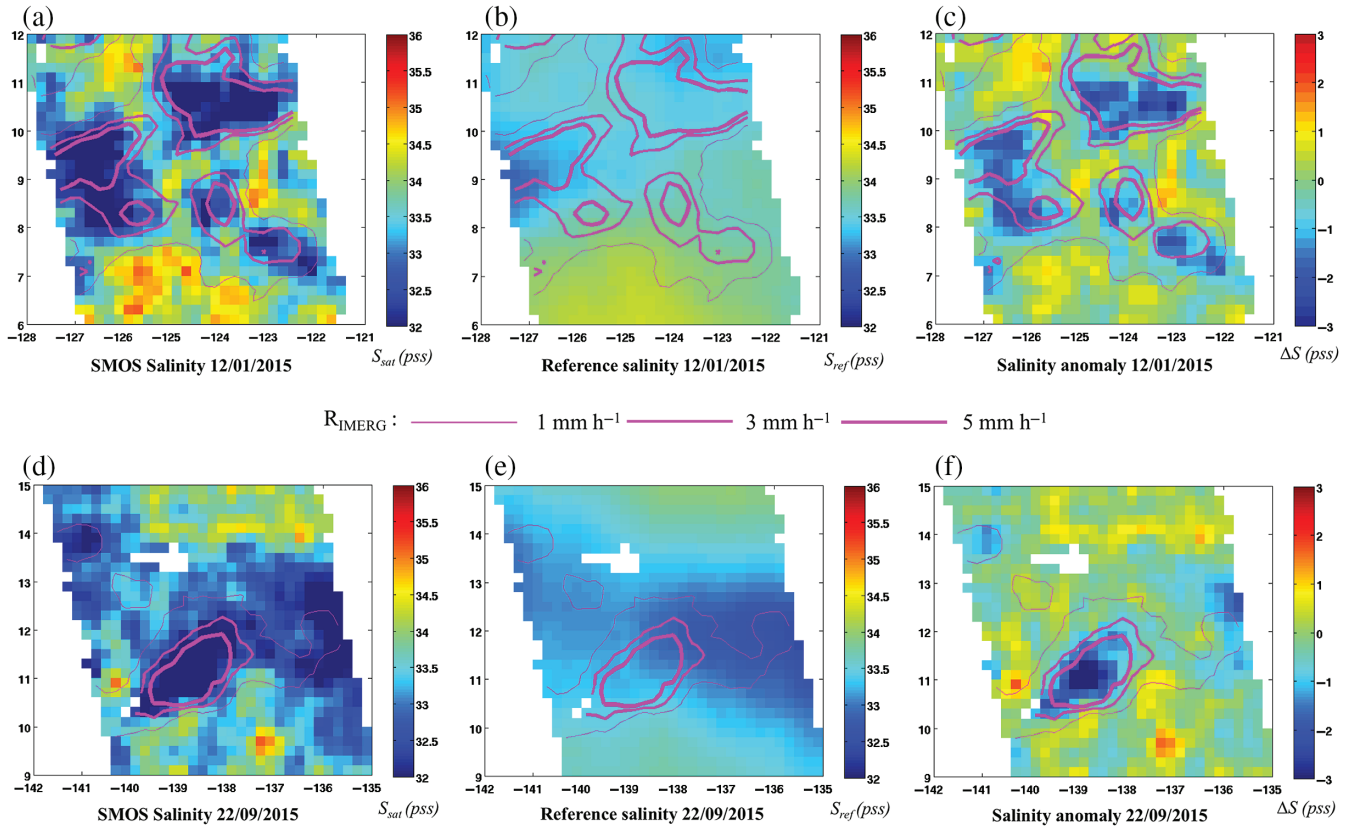

FIGURE 5 SMOS ascending swath for two study cases, (a–c) January 12, 2015 and (d–f) September 22, 2015, in order to illustrate the use of S_{sat} (a, d) in the derivation of S_{ref} (b, e) and the computation of ΔS (c, f). Magenta isolines are selected contours of R_{IMERG} (1, 3 and 5 mm/hr)

from the average of the adjacent pixels, the average being weighted by the inverse of the surface of each original pixel entering in the 0.2° × 0.2° grid. The 0.2° resolution has been chosen as being intermediate between the original sampling of the products (0.1° to 25 km) and the true resolution of PMW-derived parameters (up to 4 km × 6 km and up to 15 km × 15 km for sounders).

Temporal collocations are made between closest available products, within a given range of time. SMOS passes are very often close to SSMIS passes; in about 45% of the cases, SMOS and SSMIS passes are less than 15 min apart (Figure 1). The temporal shift between SMOS and SSMIS (principally F17 for 2014–2015–2016 period) satellites are unequal as function of the considered year. Due to the orbital drift of SSMIS satellites, the closest collocations occurred in 2015.

3 | RETRIEVAL OF RR FROM SATELLITE SALINITY

3.1 | Training phase

3.1.1 | ΔS versus R_{PMW} relationship

Comparisons between ΔS and R_{PMW} show slopes in the same range as the ones reported in Boutin et al. (2016). Nevertheless, the scatter plots obtained with MHS RR (R_{MHS}) are much noisier than the ones obtained with SSMIS (r = −0.31 and −0.43 respectively, see Figure 6). SSMIS satellites use a wide spectrum of frequencies (19–183 GHz) to extract information on RR using emission and scattering properties by rain. MHS satellites have a narrower spectrum (between 89 and 183 GHz, for AMSU-B) so that RRs are derived using only scattering properties. Therefore, R_{SSMIS} are expected to be more precise than R_{MHS} (Vila, Ferraro, & Joyce, 2007) which is in line with results shown in Table 1. In the following the relationship between SMOS ΔS and RR measurements is derived using only R_{SSMIS} collocations (Figure 6; statistics are indicated in the first part of Table 1). It is remarkable that the relationship obtained with SSMIS RR (R_{SSMIS}) is independent of the smoothing, suggesting that the relationship is linear up to at least 7 mm/hr. Smoothing over 1° × 1° significantly increases the correlation (r) between the two variables (r = −0.43 without smoothing and r = −0.55 with 1° × 1° smoothing) and decreases the RMSD (RMSD = 0.51 mm/hr without smoothing and RMSD = 0.29 mm/hr with 1° × 1° smoothing).

3.1.2 | R_{SMOS} retrieval

In order to retrieve RR from SMOS data, we apply the inverse of the slope between ΔS and R_{SSMIS} (−0.27 pss (mm/hr)$^{-1}$; Table 1 first line). Thus, the equation used to retrieve unbiased Gaussian-shaped RR from SMOS ΔS (R_{SMOS_G}) is:

$$\mathbf{R_{SMOS\_G} = -3.70 \times \Delta S - 0.04}. \quad (3)$$

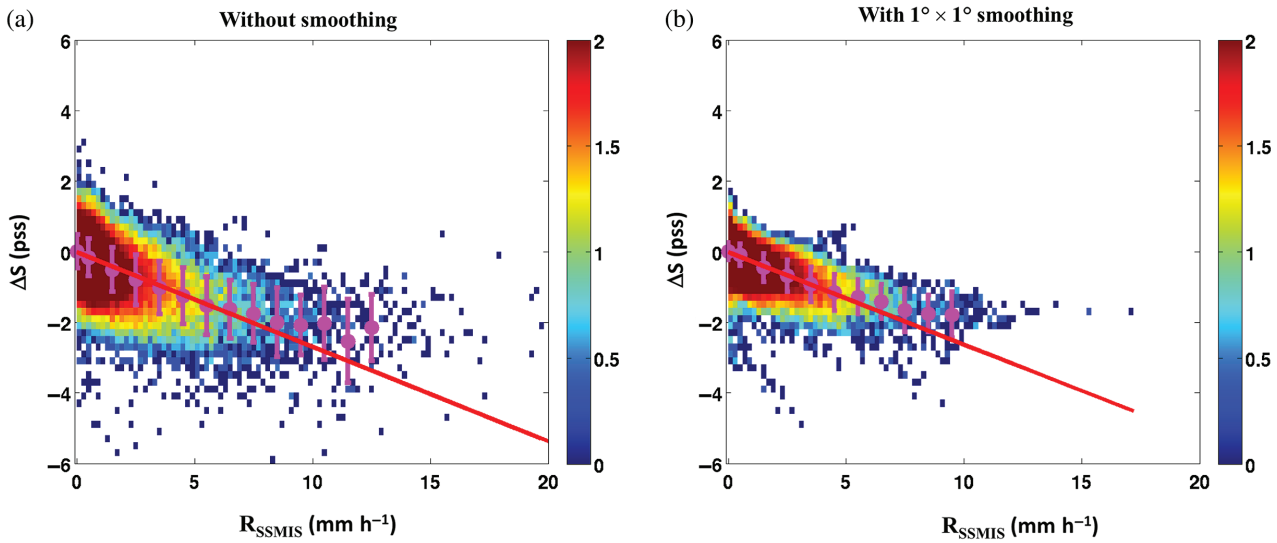

FIGURE 6 ΔS versus R_{SSMIS} in rainy regions as detected by R_{IR} (see Section 2.2.1. for the definition) for the 2015 year (a) without smoothing, and (b) with 1° × 1° smoothing. Mean and standard deviation computed for each R_{SSMIS} classes and with R_{SSMIS} reference. The colour scale corresponds to the $\log_{10}$ of the number of occurrences

TABLE 1 Statistics on the relationship between ΔS and R_{PMW} with all satellites with SSMIS and MHS computed during the training year (RR is given in mm/hr)

Satellites	Statistics	Without smoothing	With 1° × 1° smoothing
SSMIS	Best-fit	$\Delta S = -0.27\ R_{SSMIS} - 0.01$	$\Delta S = -0.26\ R_{SSMIS} - 0.01$
	r	−0.43	−0.55
	RMSE (pss)	0.51	0.29
	N	251 317	247 868
MHS	Best-fit	$\Delta S = -0.12\ R_{MHS} - 0.05$	$\Delta S = -0.14\ R_{MHS} - 0.04$
	r	−0.31	−0.44
	RMSE (pss)	0.53	0.30
	N	33 691	33 156

Best-fit obtained with linear regressions. Root-mean-square error, $RMSE = \sqrt{\overline{(\Delta S_{estim} - \Delta S)^2}}$. $r = \frac{cov(\Delta S, R_{SSMIS})}{\sigma_{\Delta S}\sigma_{R_{SSMIS}}}$.

R_{SMOS_G} obtained with this relationship are noisy because of SMOS S_{sat} noise. This can generate numerous negative rain values derived from SMOS freshening and consequently R_{SMOS_G} distribution largely differs from the SSMIS log-normal-shaped rain distribution (Figure 7a). In order to reduce the effect of SMOS measurement noise and to correct the distribution of SMOS RR estimates, we use a heuristic methodology. It consists in multiplying R_{SMOS_G} by the probability that R_{SSMIS} is above a threshold taken as the RR value for which the difference between R_{SMOS_G} CDF and R_{SSMIS} CDF is maximum. This probability is related to the value of ΔS and to the lower part of the ΔS distribution in a 3° × 3° area. The latter is characterized by the 0.1 quantile of ΔS distribution ($Q_{0.1}$: the ΔS value below which 10% of ΔS in the 3° × 3° area occur) in the 3° × 3° area surrounding the considered pixel, bearing in mind that rainy systems usually detected by satellite measurements in the ITCZ are wider than 50 km.

In order to illustrate how this method works, Figure 7b shows the difference between R_{SMOS} and R_{SSMIS} cumulative distribution functions (CDF) in two cases: SMOS RR computed with and without IR filtering. Without IR filtering we observe that the CDF difference is maximum for R equal to 0 mm h^{-1}. This is expected due to: (i) the fact that percentage of non-rainy events (85%) is large in comparison to percentage of rainy events (15%), and (ii) R_{SSMIS} is always positive contrary to R_{SMOS_G}. In this case, the large majority of negative RR are generated by non-rainy conditions. Hence our heuristic method would have weighted R_{SMOS_G} by $P(R_{SSMIS} > 0 \mid \mathbf{\Delta S}$ and $Q_{0.1})$. However, the PEALS algorithm uses an IR filtering that changes the ratio of rainy/non-rainy events. After IR filter, the percentage of rainy events increases and reaches 30%. In this case the CDF difference is maximum for R close to 0.6 mm h^{-1}. This is why we set the probability threshold ($P\{RR > 0.6$ mm $h^{-1}\}$) in order to equalize R_{SMOS} and R_{SSMIS} distributions. Using $\Delta S/R_{SSMIS}$ colocations during the 2015 year, we determine the probability that RR exceed 0.6 mm h^{-1} ($P\{RR > 0.6$ mm $h^{-1}\}$) as a function of ΔS and of $Q_{0.1}$. By weighting R_{SMOS_G} with $P(R_{SSMIS} > 0.6 \mid \mathbf{\Delta S}$ and $Q_{0.1})$, Figure 7a shows that it is possible to correct the distribution of rain estimates obtained with SMOS.

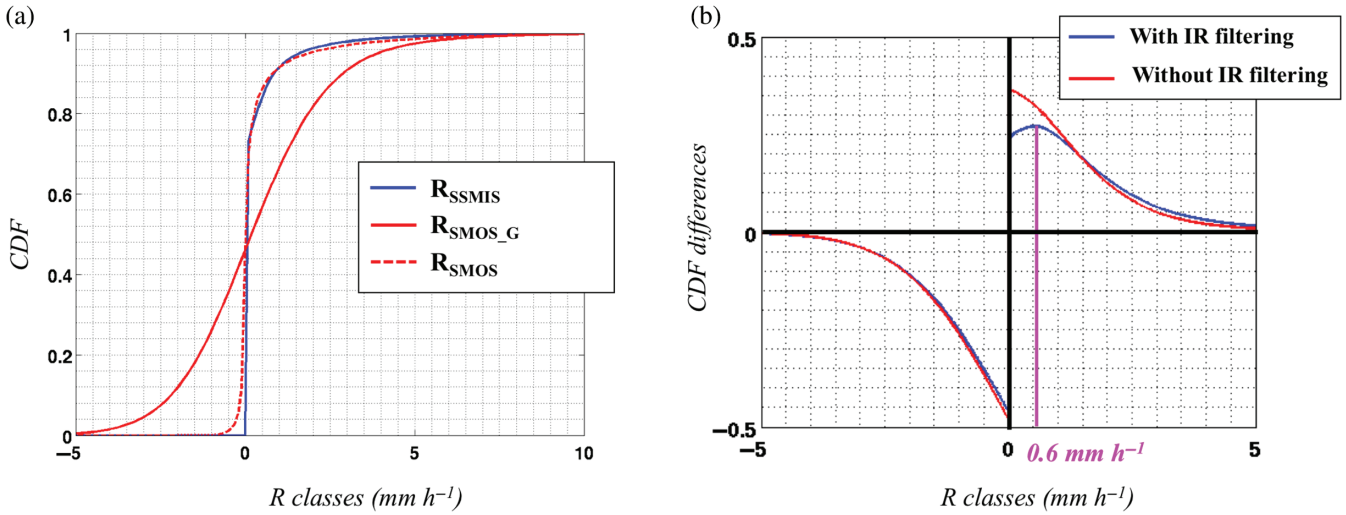

FIGURE 7 (a) Normalized cumulative distribution functions for R_{SSMIS} (blue full-line), R_{SMOS_G} (red full-line), R_{SMOS} (red dashed-line) (only the case with IR filtering is considered). (b) Differences between R_{SMOS} and R_{SSMIS} CDF with IR filtering (blue) and without IR filtering (red)

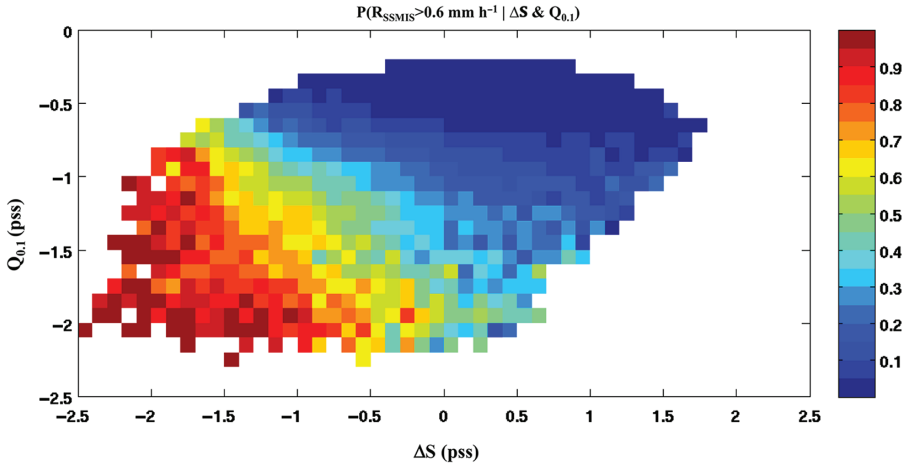

FIGURE 8 Correction function computed over ITCZ during training period (2015), representing $P(R_{SSMIS} > 0.6)$ (colour bar) as function of $Q_{0.1}$ and ΔS

Using this approach, the equation used to retrieve unbiased log-normal-shaped RR from SMOS ΔS is:

$$\mathbf{R_{SMOS} = R_{SMOS\_G} \times P(R_{SSMIS} > 0.6 \mid \Delta S \& Q_{0.1})}. \quad (4)$$

$P(R_{SSMIS} > 0.6 \mid \Delta S$ and $Q_{0.1})$ is computed over ITCZ for the training period and integrated in a correction function. As expected and shown in Figure 8, the probability of observing RR higher than 0.6 mm h^{-1} increases when ΔS decreases and when $Q_{0.1}$ decreases. For a given $Q_{0.1}$ value, probability increases with ΔS. For a given ΔS value, the probability increases with $Q_{0.1}$.

3.1.3 | Verification of R_{SMOS}

In order to conduct a first evaluation of R_{SMOS}, we compare R_{SMOS} and R_{SSMIS} with two different resolutions. In addition to the 0.2° × 0.2° resolution, rain estimates are smoothed over 1° × 1° resolution. That corresponds to the typical size of the smallest large-scale convective systems in the ITCZ area (Houze, 2004; Waliser & Gautier, 1993) that will thus be sampled.

A typical example of R_{SMOS} obtained with and without smoothing is presented in Figure 9. In this case, the temporal shift between R_{SMOS} and R_{SSMIS} is small; SMOS flew over the area 12–14 min after SSMIS. R_{SMOS} is qualitatively in good agreement with R_{SSMIS} with and without smoothing. Nevertheless, in this case, R_{SMOS} seems to miss the lowest RR located at the edge of rain cells and thus underestimates RR after smoothing.

We compare R_{SMOS} and R_{SSMIS} with a pixel-to-pixel analysis in 2015 in a 15 min time interval with both resolutions, including rain and rain-free scenes (Figure 10a and Table 2). Results show a very good agreement between R_{SMOS} and R_{SSMIS} (r = 0.64 and 0.73 without and with smoothing respectively; RMSD = 0.62 mm h^{-1}; with 1° × 1° smoothing: RMSD = 0.42 mm h^{-1}) (see Table 2).

3.2 | Validation and seasonal variability

3.2.1 | Pixel-to-pixel comparison of SMOS and SSMIS RR

In order to test the validity of the PEALS algorithm, we compute statistics for R_{SMOS} and R_{SSMIS} during the validation

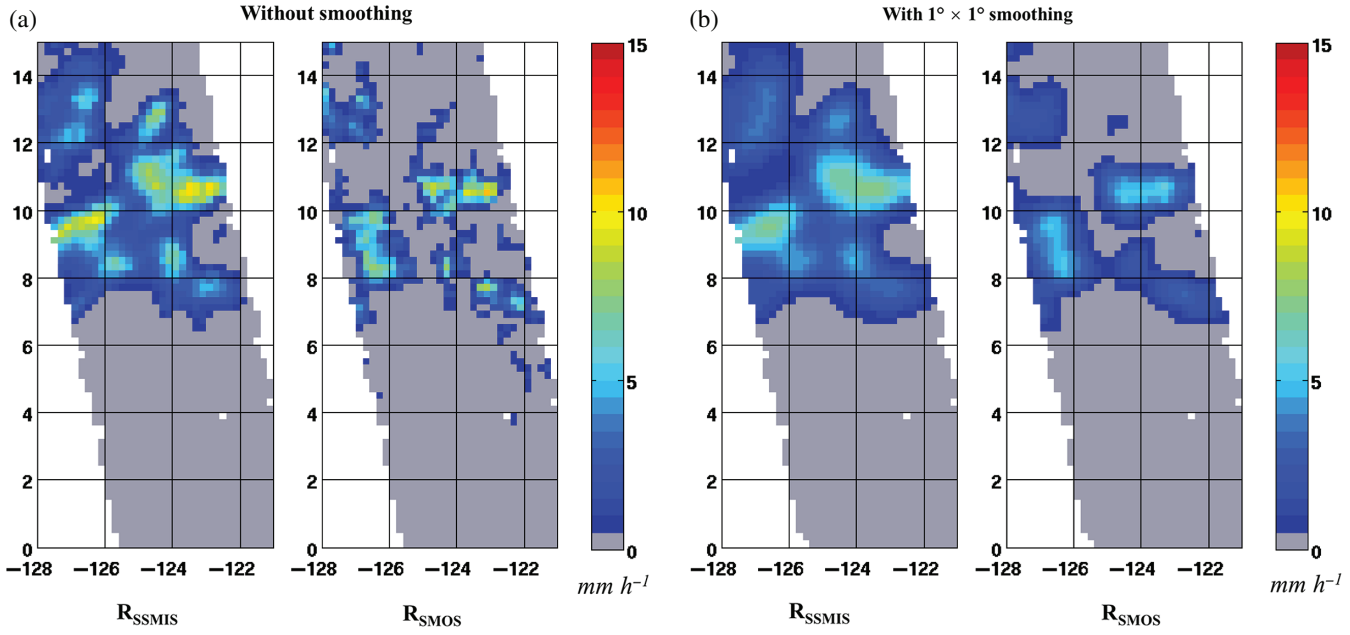

FIGURE 9 (a, b) R_{SMOS} for a case-study (January 12, 2015) in comparison with R_{SSMIS} for different smoothing levels. SMOS pass (1412 UTC) is 12–14 min after SSMIS

period. During the second part of the validation period (June and July 2016), differences due to the high cyclonic activity (north of 9°N) are observed. As shown in Figure 11, during the *Georgette* cyclone study case SMOS RR are lower than IMERG RR. It is not clear at this stage if it is due to the linear approximation assumed in the relationship between R_{SSMIS} derived with the GPROF algorithm and ΔS or to inaccurate ECMWF tracking and wind speed for tropical cyclones (ECMWF, 2004) that are potential source of errors for salinity estimates in their immediate vicinity. Because of these uncertainties in the vicinity of cyclones, we have restricted the area in which we investigate measurements to 0–9°N between June and July 2016. Results from this analysis for time shift less than 15 min are shown in Table 2 and Figure 10b. They are slightly noisier than the ones obtained during the training period. The correlation for the validation period is 0.62 (0.72 with 1° × 1° smoothing), very close to the one of the training period (0.64; 0.73 with 1° × 1° smoothing); the comparison remains a little noisier considering the RMSD (RMSD = 0.64 mm h^{-1} instead of 0.62 mm h^{-1} in 2015; with 1° × 1° smoothing: RMSD = 0.45 mm h^{-1} instead of 0.42 mm h^{-1} in 2015). During the whole study period, the RMSD of SMOS RR with respect to rainy SSMIS RR is 1.04 mm h^{-1} for SSMIS RR less than 2 mm h^{-1} (87% of SSMIS rainy RR), 1.31 mm h^{-1} for SSMIS RR less than 5 mm h^{-1} (97% of SSMIS rainy RR). This RMSD is larger for higher RR: 3.28 mm h^{-1} for SSMIS RR greater than 2 mm h^{-1} (13% of SSMIS rainy RR) and 4.91 mm h^{-1} for SSMIS RR greater than 5 mm h^{-1} (3% of SSMIS rainy RR).

3.2.2 | Monthly variability of rain rate

In addition to validating R_{SMOS} at short time-scale, we compare monthly averages of R_{SMOS} with R_{SSMIS} and R_{IMERG}. SSMIS monthly averages are estimated by selecting only R_{SSMIS} in 15 min time interval from R_{SMOS}. IMERG monthly averages are estimated by selecting only the closest R_{SMOS} and R_{IMERG} estimates (in space and time; only with SSMIS as closest PMW). We take into account rainy and non-rainy pixels. The monthly average in a given pixel is equal to the rain accumulation divided by the number of observations. Since the number of observations during 1 month varies from one pixel to another, the average has been preferred.

Hovmüller plots in which monthly R_{SMOS} and R_{SSMIS} are averaged for each degree of latitude between 180°W and 110°W longitude ($<R_{SMOS}>$ and $<R_{SSMIS}>$) show SMOS ability to reproduce SSMIS seasonality as well as rainfall average intensity (Figure 12a,c). The monthly time series of the average over the whole region (Figure 13a,b) confirm a good comparison even though slightly larger differences in monthly R_{SMOS} and R_{SSMIS} are observed from July to October 2014 and in June–July 2016. During the latter period, the differences are due to the high cyclonic activity north of 9°N mentioned earlier. Correlation of SMOS Hovmüller pixels with SSMIS pixels computed in the restricted area (as defined above) highlight the good agreement between SMOS and SSMIS monthly rain estimates (the coefficient of correlation of Hovmüller pixels is r = 0.89, RMSD = 0.07 mm h^{-1} and $<R_{SMOS}> = 1.03<R_{SSMIS}> + 0.00$).

This analysis was also conducted with R_{IMERG}. Figure 12b,d indicates that as for R_{SSMIS}, the R_{IMERG} Hovmüller plot also present a good agreement with R_{SMOS} (r = 0.92 and RMSD = 0.06 mm h^{-1}). However, as shown on Figure 13c,d and confirmed by the relationship between R_{SMOS} and R_{IMERG} Hovmüller ($<R_{SMOS}> = 0.90<R_{IMERG}> + 0.01$), R_{SMOS} is biased in comparison with R_{IMERG}.

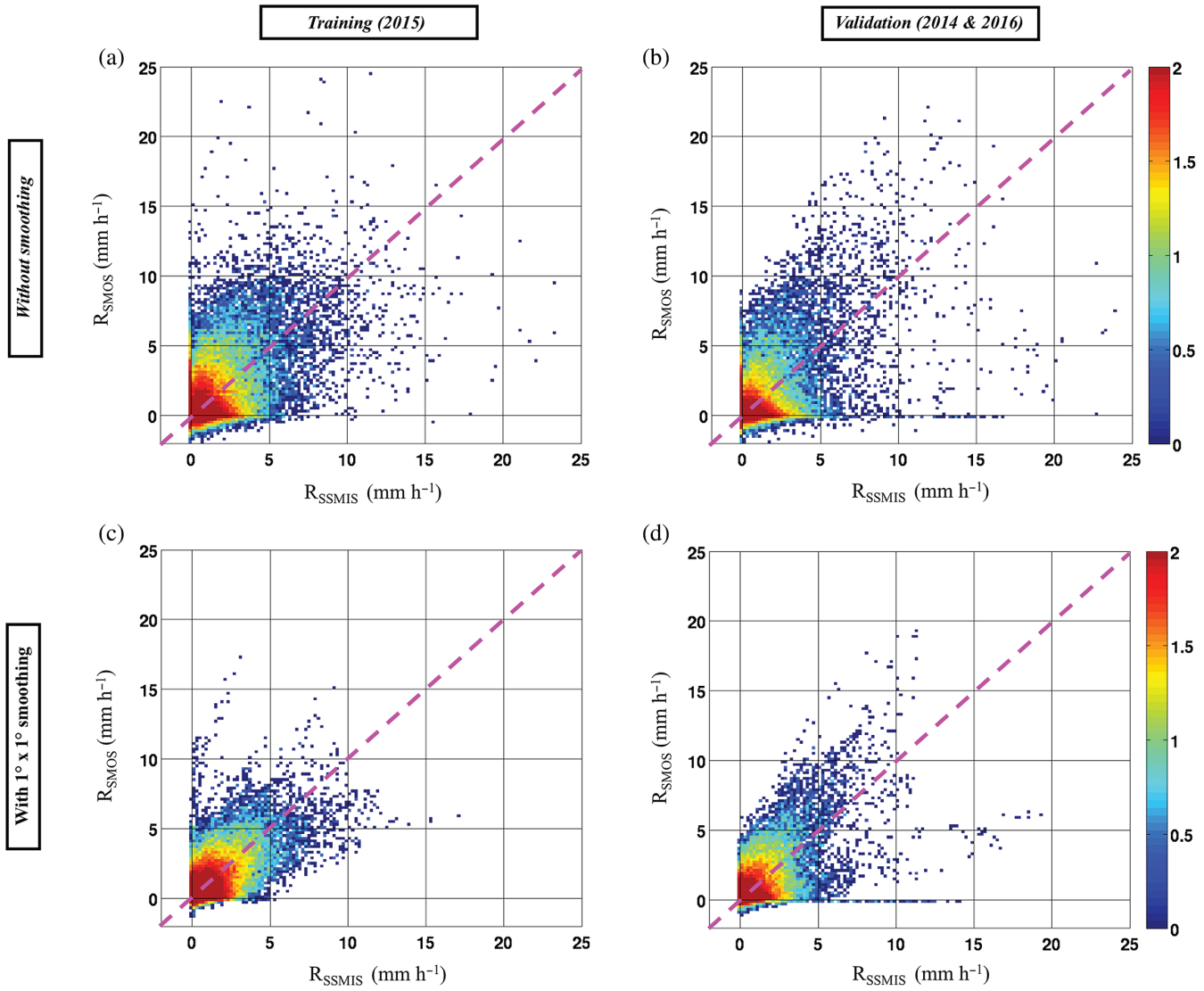

FIGURE 10 Scatterplots between R_{SMOS} and R_{SSMIS}: (a) without smoothing, during training period; (b) without smoothing, during validation period; (c) with 1° × 1° smoothing, during training period; (d) with 1° × 1° smoothing, during validation period. Magenta dashed-line: $R_{SMOS} = R_{SSMIS}$. The colour scale corresponds to the $\log_{10}$ of the number of occurrences

TABLE 2 Statistics on the comparison between R_{SMOS} and R_{SSMIS} (from 0° to 15°N between August 2014 and May 2016, and from 0° to 9° in June and July 2016)

Years	r	RMSD (mm/hr)	N
2015 (without smoothing)	0.64	0.60	532 706
2014 and 2016 (without smoothing)	0.62	0.63	353 110
2015 (with 1° × 1° smoothing)	0.73	0.41	525 244
2014 and 2016 (with 1° × 1° smoothing)	0.71	0.44	348 644

$$RMSD = \sqrt{\overline{(R_{SMOS} - R_{SSMIS})^2}}.\ r = \frac{cov(R_{SMOS}, R_{SSMIS})}{\sigma_{R_{SMOS}} \sigma_{R_{SSMIS}}}.$$

3.3 | Validation with SMAP and influence of R_{SSMIS} availability

3.3.1 | SMOS/SMAP comparison

Figure 14 summarizes comparisons between SMOS and SMAP parameters collocated in a 15 min time interval from January to July 2016. Associated statistics are reported in Table 3. SMOS S_{sat} and SMAP S_{sat} are in good agreement (Figure 14a) even though they are shifted by 0.26 pss on average (Figure 14a and Table 3). SMOS and SMAP salinity have slightly different standard deviation (STD) values, suggesting that SMOS SSS are noisier than SMAP SSS (Figure 14b and Table 3). Assuming that the total variance measured by SMOS ($\sigma^2_{tot\ SMOS}$) and by SMAP ($\sigma^2_{tot\ SMAP}$) is equal to the sum of the variance due to instrumental noise

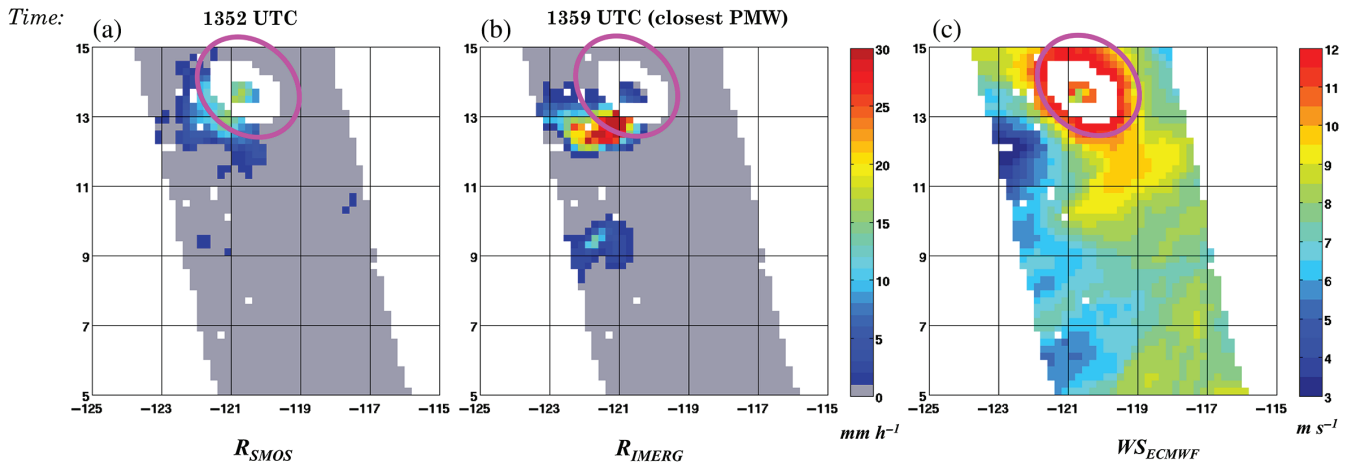

FIGURE 11 Study case, July 23, 2016, Cyclone *Georgette*: (a) R_{SMOS} rain estimates; (b) R_{IMERG} rain estimates; (c) ECMWF wind speed. Magenta circle: flagged area due to wind speeds higher than 12 m/s

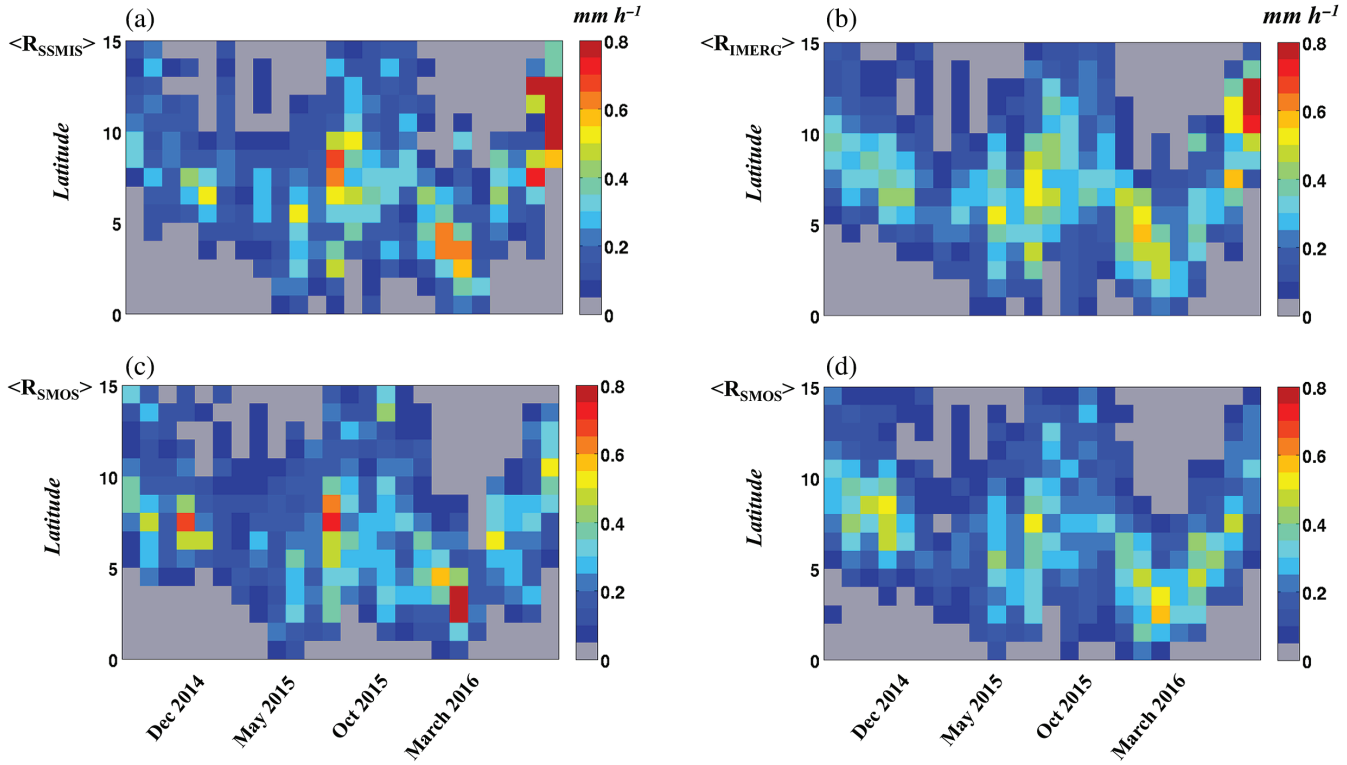

FIGURE 12 (a, c) SSMIS collocated with SMOS in 15 min time interval with (a) Hovmüller diagrams of R_{SSMIS} and (c) Hovmüller diagrams of R_{SMOS}; (b, d) IMERG collocated with SMOS (but only with SSMIS as nearest collocated rain satellite) with (b) Hovmüller diagrams of R_{IMERG} and (d) Hovmüller diagrams of R_{SMOS}. With an orthogonal regression $<R_{SMOS}> = 1.03<R_{SSMIS}> + 0.00$ (r = 0.89; RMSD = 0.07) and $<R_{SMOS}> = 0.90<R_{IMERG}> + 0.01$ (r = 0.92; RMSD = 0.06) after exclusion of pixels above 9°N during the last 2 months of the study period

(σ^2_{inst}) and due to natural variance (σ^2_{nat}), we can derive from their total variance the error of SMAP S_{sat} relative to the one of SMOS S_{sat}, with the following equations:

$$\sigma^2_{tot\ SMOS} = \sigma^2_{inst\ SMOS} + \sigma^2_{nat},$$
$$\sigma^2_{tot\ SMAP} = \sigma^2_{inst\ SMAP} + \sigma^2_{nat},$$
$$\sigma^2_{inst\ SMOS} = \sigma^2_{inst\ SMAP} + \sigma^2_{tot\ SMOS} - \sigma^2_{tot\ SMAP},$$
$$\sigma^2_{inst\ SMOS} = \sigma^2_{instSMAP} + 0.80^2 - 0.75^2,$$
$$\boldsymbol{\sigma^2_{instSMOS} = \sigma^2_{instSMAP} + 0.08}.$$

In the ITCZ region, the error on individual SMOS S_{sat} is estimated to be 0.57 pss (as measured over the whole study area during 2015) resulting in an error on SMAP S_{sat} estimated to be 0.49 pss.

In spite of the shift between SMOS and SMAP SSS distributions, the mean and the distribution of ΔS for SMOS and SMAP are very close (Table 3 and Figure 14d). Consequently, R_{SMAP} and R_{SMOS} are really comparable as shown with the scatter plot (Figure 14e), their statistical distributions (Figure 14f) and their mean values (Table 3).

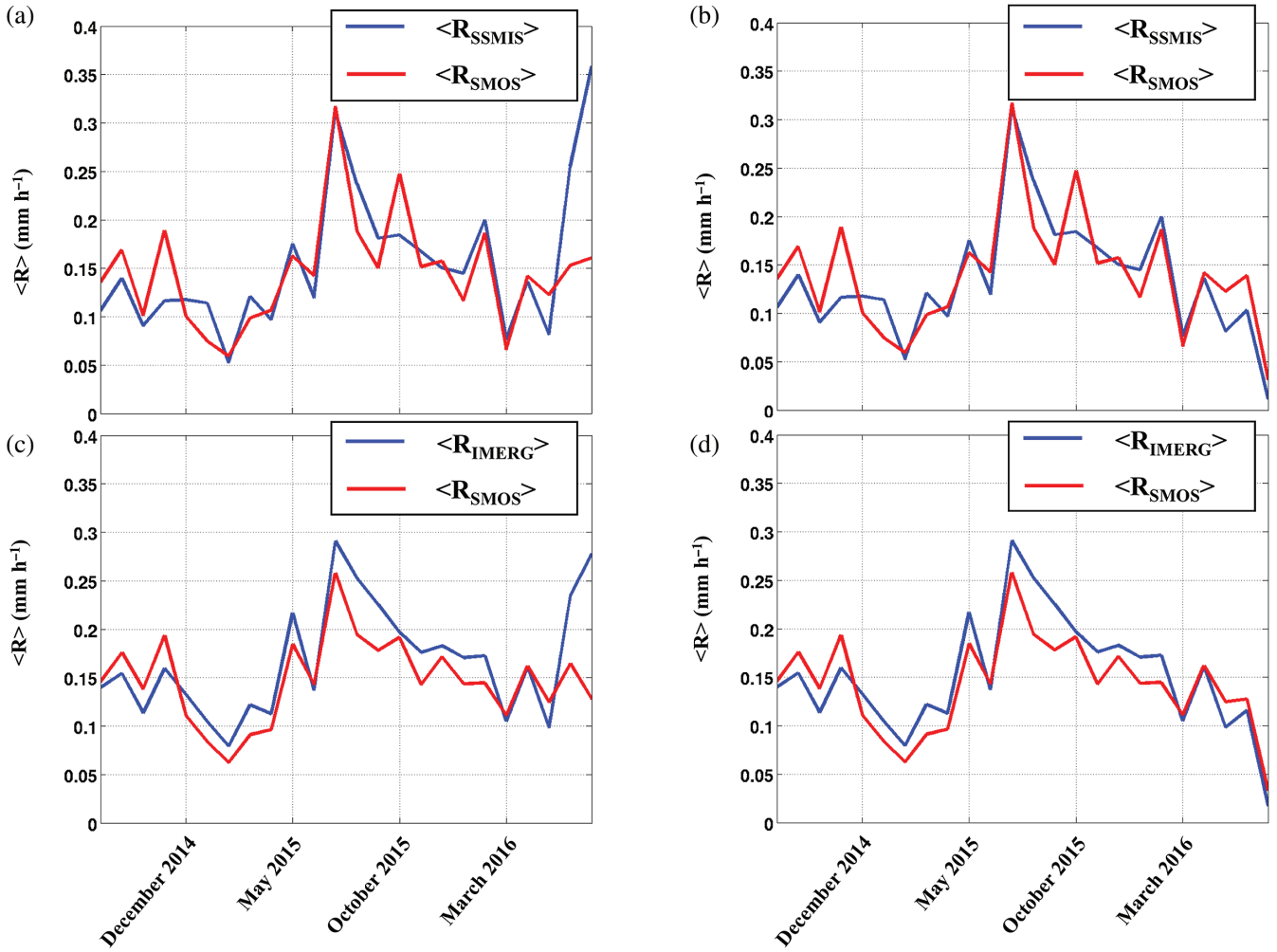

FIGURE 13 (a, c) During the whole period and for the whole study area: (a) monthly RR averages for SMOS and SSMIS (SSMIS collocated with SMOS in 15 min time interval) and (c) monthly RR averages for SMOS and IMERG (only with SSMIS as nearest collocated rain satellite). (b, d) For the restricted area (without measurements between 9° and 15°N during June to July 2016): (b) monthly RR averages for SMOS and SSMIS (SSMIS collocated with SMOS in 15 min time interval) and (d) monthly RR averages for SMOS and IMERG (only with SSMIS as nearest collocated rain satellite)

3.3.2 | Influence of the availability of R_{SSMIS} onto R_{IMERG} estimation

The dependency of the correlation between R_{SMOS} and R_{SSMIS} (and R_{IMERG}) on the temporal shift with the nearest SSMIS satellite is studied during the whole study period. The main target of the merged rain product R_{IMERG} is to compensate for the lack of information concerning rain due to the lack of PMW at a given time by morphing of rain cell with the help of IR rain estimates. We test the contribution of IMERG merging by comparing the correlation between R_{SMOS} and the closest R_{IMERG} ($r_{R_{SMOS}/R_{IMERG}}$) as a function of increasing temporal shift between SMOS and closest SSMIS (Figure 15; only cases with SSMIS satellite as nearest PMW satellite are considered). We subtract from them the correlation between R_{SMOS} and R_{IR} ($r_{R_{SMOS}/R_{IR}}$) that is considered as the minimum correlation that could be reached between SMOS and IMERG. During the whole study period, as expected, the difference between $r_{R_{SMOS}/R_{IMERG}}$ and $r_{R_{SMOS}/R_{IR}}$ decreases less rapidly when Δt between SMOS and the nearest SSMIS satellite increases than the difference between $r_{R_{SMOS}/R_{SSMIS}}$ and $r_{R_{SMOS}/R_{IR}}$. This shows that R_{IMERG} presents a better consistency with R_{SMOS} when no R_{SSMIS} is shortly available, even though it is not able to provide the same level of correlation as the one obtained between R_{SMOS} and R_{IMERG} when R_{SSMIS} are available within a very short temporal radius (Figure 15).

Figure 16 illustrates the very good consistency of SMOS, SMAP and IMERG RR for very short time shifts between all radiometric measurements (less than 15 min), and the worse consistency between IMERG and salinity-derived RR for the largest temporal shift between nearest SSMIS and SMOS or SMAP.

4 | DISCUSSION AND CONCLUSION

Taking advantage of the relationship between ΔS from SMOS and rain intensity from PMW satellites, we have developed a retrieval algorithm (PEALS) that estimates RR from SMOS measurements. In order to avoid freshening due to other processes than rainfall, we only retrieve SMOS RR in the vicinity of regions identified as rainy by IR measurements. Because

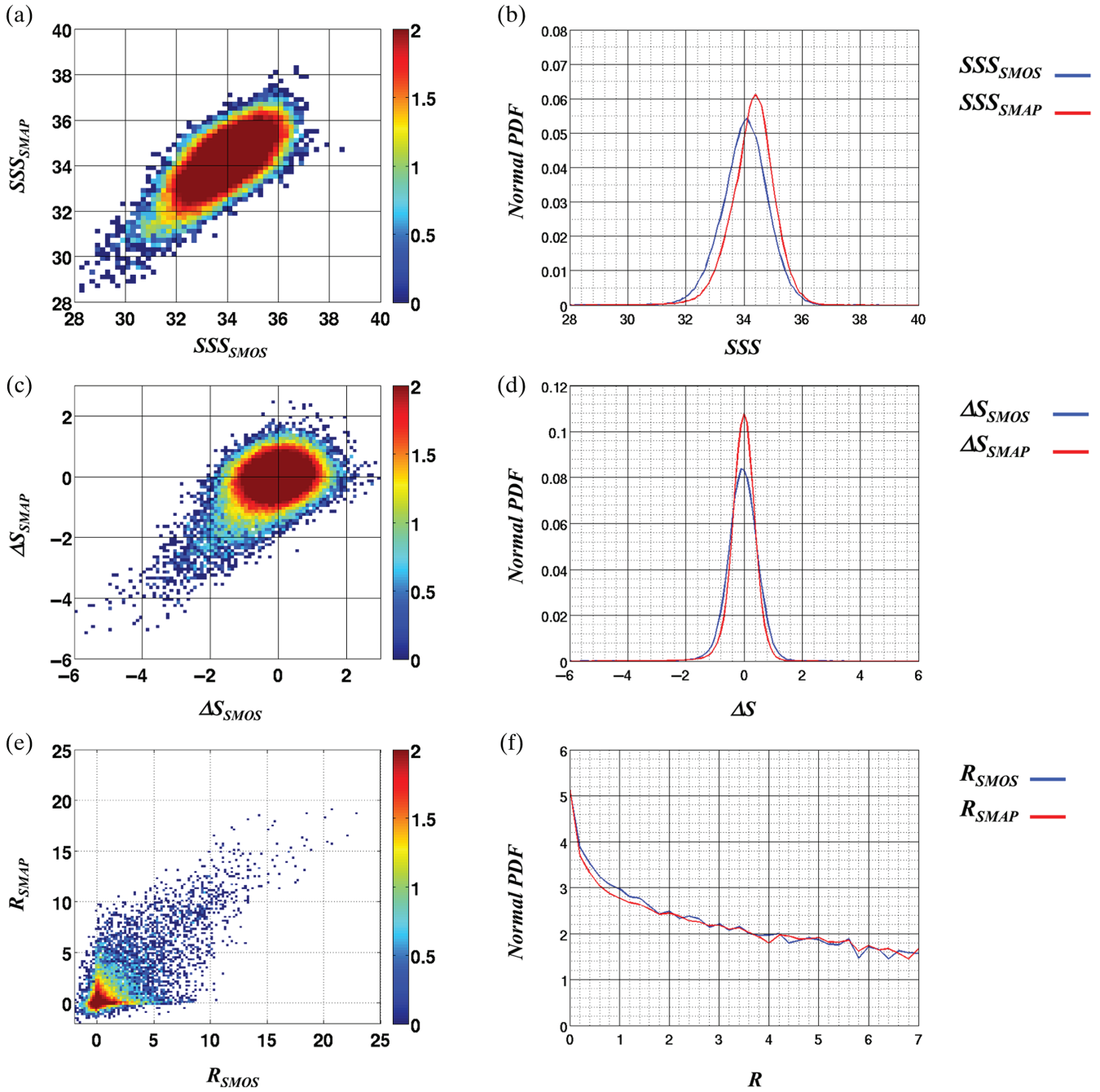

FIGURE 14 (a, c, e) Scatterplots between SMOS and SMAP data, and (b, d, f) distributions, collocated within less than 15 min (January to July 2016): (a, b) salinity; (c, d) ΔS; (e, f) rain rate. The colour scale corresponds to the $\log_{10}$ of the number of occurrences

of SMOS SSS noise, numerous negative RR are retrieved when just taking the inverse of the ΔS(RR) relationship. In order to correct for this flaw, a heuristic scheme is applied. The algorithm finally adopted consists of estimating at the grid-point level the instantaneous RR from the SMOS freshening by using local information surrounding the considered grid point.

Since the relaxation time of the freshening is extremely short (of the order of a few hours) in comparison with the satellite revisiting times, successive SMOS satellite passes sample independent rain events. Monitoring the temporal evolution of a rain event is only possible owing to satellite passes close in time (e.g. SMOS, SMAP, SSMIS). Given the important theoretical uncertainties that exist to account for the physics of the ocean surface freshening by rain, we have chosen to establish an empirical model that accounts

TABLE 3 Statistics on the comparison between SMOS and SMAP (collocated within 15 min time interval; January to July 2016; without smoothing)

Satellite	Statistics	S_{sat} (pss)	ΔS (pss)	R (mm/hr)
SMOS	*Mean*	34.03	−0.05	0.13
	std	0.80	0.52	0.81
SMAP	*Mean*	34.29	−0.04	0.13
	std	0.75	0.45	0.77

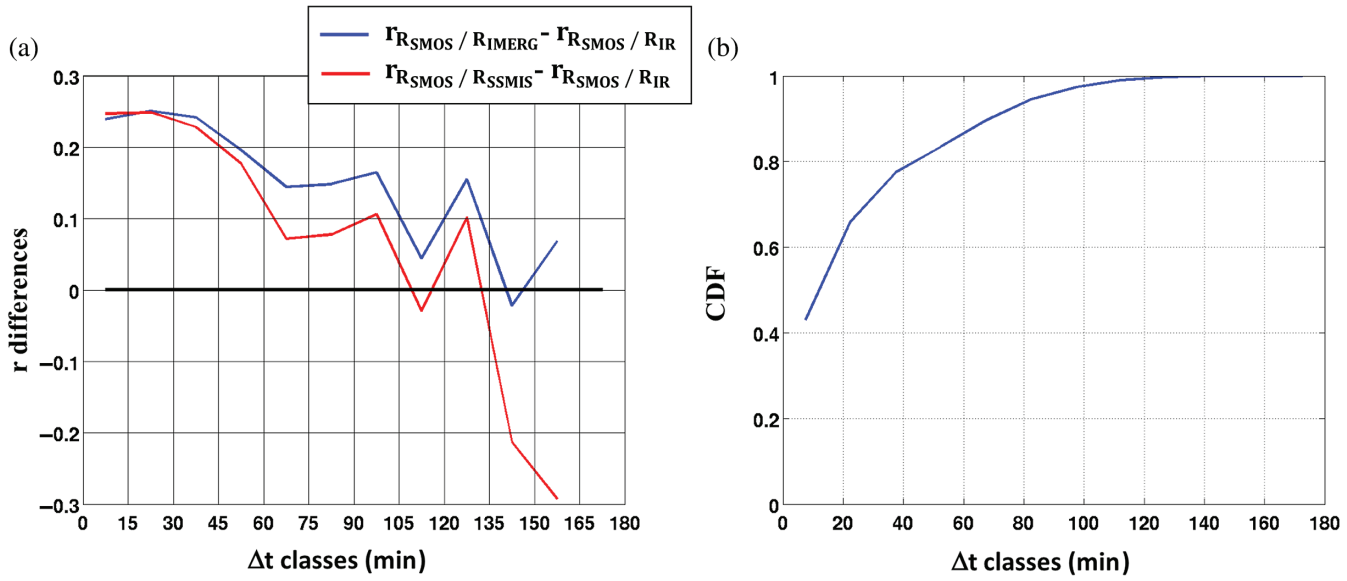

FIGURE 15 (a) Correlation between R_{SMOS} and R_{IMERG} minus correlation between R_{SMOS} and R_{IR} (blue line); correlation between R_{SMOS} and R_{SSMIS} minus correlation between R_{SMOS} and R_{IR} (red line), as function of temporal shift (Δt) between SMOS and nearest (in time) SSMIS. Size of Δt classes = 15 min. (b) CDF of number of pixels as function of temporal shift (Δt) between SMOS and nearest (in time) SSMIS

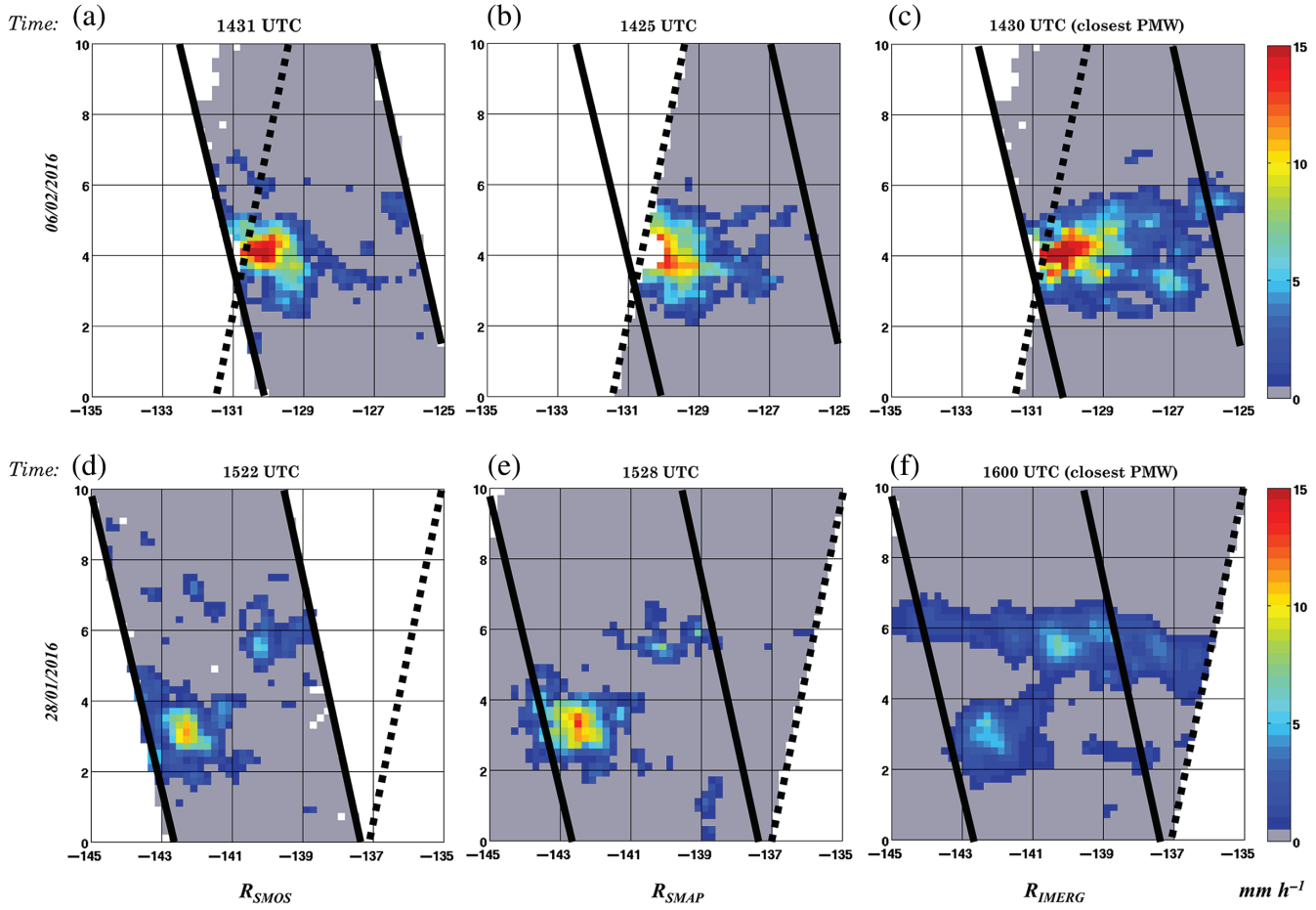

FIGURE 16 (a–c) Case-study of 6 February 2016, short temporal shift between SMOS/SMAP and the closest PMW: (a) R_{SMOS}; (b) R_{SMAP}; (c) R_{IMERG}. (d–f) Case-study of 28 January 2016, long temporal shift between SMOS/SMAP and the closest PMW: (d) R_{SMOS}; (e) R_{SMAP}; (f) R_{IMERG}.

for observations. This empirical approach is made possible by the presence of SMOS data co-located with microwave satellite data to estimate the RR. Several assumptions behind this algorithm are recalled below: (i) We determine an instantaneous RR. The correlation between freshening and RR decreases very rapidly because the freshening relaxes very quickly (see references in Boutin et al. (2016)). (ii) An estimate of non-rainy SSS can be obtained from the 3° × 3°

data surrounding the grid node under consideration. (iii) The ΔS(RR) model is linear. Theoretical models present a broad spectrum of variation that depends on the underlying parameters mainly related to micro-turbulence mixing mechanisms, and on environmental forcing parameters. Because SMOS measurements are relatively noisy (at least 0.5 pss) and because forcing parameters were not easily available, a linear approach appeared to be appropriate at the first order. (iv) The PEALS model is calibrated using GPROF2014 SSMIS RR provided in the IMERG version 3 product. The GPROF2014 algorithm overestimates the number of low RR pixels (Kidd, Panegrossi, Ringerud, & Stocker, 2017). In addition, as shown by Hilburn and Wentz (2008), significant differences exist between UMORA and GPROF which may explain part of the nonlinear behaviour at high RR observed in Figure 6, as discussed below. (v) The model is not dependent on wind speed. The current model does not include a wind speed dependence explicitly in the equation. This is related to the fact that the ECMWF model does not provide a reliable wind speed under rain cells, and very few reliable satellite observations of wind under rain cells are available. This is a strong assumption that should be further investigated in the future. Locally *in situ* measurements in rain puddles and modelling studies suggest a strong influence of rain-induced freshening intensity with wind speed (Asher et al., 2014; Bellenger et al., 2016; Drushka et al., 2016). However, rain puddles are expected to be very heterogeneous in a 50 km × 50 km satellite pixel and local wind speed dependency is expected to be nonlinear. Hence, the dependency of satellite rain-induced freshening with wind speed is highly uncertain. In our study, we exclude very low and very high wind speeds and we consider only situations where ECMWF wind speeds are moderate (3–12 m/s) for which drifter measurements collocated with satellite RR and satellite wind speeds do not suggest very large variations (Boutin et al., 2014).

Correlation between SMOS and PMW RR is much larger than between SMOS and IR RR (Figure 15). Both instantaneous and monthly SMOS RR have been validated. This qualifies SMOS for bringing additional information into an IMERG-type RR product. When SMOS and PMW satellites passes are very close in time (within 1 h), high correlation levels are recorded between the two RR, that highlight PEALS ability to reproduce a very similar rain pattern to the one observed by PMW satellites. However, this agreement deteriorates when the time shift between the two satellite passes increases and correlation between SMOS and PMW RR largely decreases. In that case, comparison of SMOS RR with IMERG merged rain products shows that morphing techniques improve the correlation. However, agreement between both rain products remains lower than the one between SMOS and PMW when the time shift is short. As the temporal shift between SMOS and nearest PMW satellite increases, SMOS provides more supplementary information on instantaneous rain rate estimates. Our approach tested on IMERG products could also be undertaken with other rain interpolated products, such as Global Satellite Mapping of Precipitation (GSMaP: Aonashi et al., 2009).

Validation of instantaneous RR derived from remotely sensed measurements is challenging. Because of the strong local variability of the rain, there is usually a poor consistency of precipitation measured *in situ* and from satellite. Time averaging of gauge measurements results in better correlations with satellite individual measurements. Particularly good agreements are observed at monthly and seasonal time-scales (Bowman, 2005; Serra & McPhaden, 2003). In order to avoid this difficulty and the lack of rain measurement over ocean in comparison with satellite measurements, RR estimates from PMW are considered as a reference in this study. Various algorithms, either using conceptual precipitation models (Hilburn & Wentz, 2008), Bayesian approach (Kummerow et al., 1996) or neural network (Zabolotskikh & Chapron, 2015), have been developed to retrieve RR from satellite PMW measurements. The PEALS algorithm has been calibrated with GPROF2014, in order to ensure consistency with IMERG v3. Hence, it may reproduce biases contained in GPROF2014 and would have to be revisited when later versions are available. Using the UMORA RR, Boutin et al. (2014) found a slope between ΔS and RR close to −0.20 pss $(\text{mm h}^{-1})^{-1}$, instead of the −0.27 pss $(\text{mm h}^{-1})^{-1}$ slope we find with GPROF2014. This comes from the different dynamics in UMORA and GPROF RR at low to moderate RR as seen in figure 10 of Hilburn and Wentz (2008). In addition, the scatter plot between ΔS and RR from UMORA appears to be closer to a linear regression than the one observed with GPROF (Figure 6) and the range of very high UMORA RR are in general lower than the one of GPROF RR. Whether the various slopes between freshening and RR could be used as independent validation for PMW RR could deserve further investigation. For instance, observed ΔS and RR relationships could be compared with the ones simulated by theoretical models (Bellenger et al., 2016; Drushka et al., 2016; Schlussel et al., 1997). In addition, atmospheric and oceanic *in situ* measurements conducted during field campaigns such as SPURS2 (SPURS-2 Planning Group, 2015) are envisaged for further validations or improvements.

This study is limited to the Pacific ITCZ region. Boutin et al. (2014) found that the relationship between ΔS and RR in the South Pacific convergence zone (SPCZ) is very close to the one for the ITCZ, so that one can reasonably expect that the methodology developed in this article will remain valid in other tropical regions. Future studies will be dedicated to adapt this methodology at higher latitudes.

We also checked the consistency between SMOS and SMAP SSS over the ITCZ area. In the region investigated, we estimate that the noise on individual SMAP SSS is 0.49 (0.57 on SMOS SSS). This noise is much less than the RMSD (0.78 pss) found by Fore et al. (2016) when comparing SMAP SSS and HYbrid Coordinate Ocean Model (HYCOM) SSS at global scale. This is because SSS retrieval is of much better quality in warm regions and because SMOS

SSS characteristics are much closer to SMAP SSS characteristics than HYCOM SSS. Actually, spatial resolutions of SMOS and SMAP are very close to 40 km and the time lag between SMOS ascending orbits and SMAP descending orbits is only a few minutes. On average, SMAP salinity is 0.26 pss higher than SMOS salinity. Nevertheless, this bias is almost corrected when salinity anomaly is considered so that RR distributions derived from SMOS and SMAP measurements are very close, both from a pixel-to-pixel analysis and from comparing monthly averages. This result validates the rain retrieval algorithm developed for SMOS with SMAP, even though, in future work, the computation of S_{ref} should be adjusted to better take into account the noise on SMAP SSS. Thus, both L-Band radiometers, SMOS and SMAP, could bring a significant supplementary coverage for rainfall to the GPM satellite constellation.

ACKNOWLEDGEMENTS

This work is supported by the ESA STSE SMOS + Rainfall (coordinated by M. Arias – ARGANS company) and by the CNES TOSCA SMOS-OCEAN projects. We thank Stéphane Marchand for his computing support, Hugo Bellenger for very fruitful exchanges about the formation of freshwater lenses and Steven Delwart and Diego Martinez (ESA) for very constructive discussions.

REFERENCES

Aonashi, K., Awaka, J., Hirose, M., Kozu, T., Kubota, T., Liu, G., … Takayabu, Y. N. (2009). GSMaP passive, microwave precipitation retrieval algorithm: Algorithm description and validation. *Journal of the Meteorological Society of Japan*, 87A, 119–136.

Arkin, P. A., & Meisner, B. N. (1987). The relationship between large-scale convective rainfall and cold cloud over the Western Hemisphere during 1982–1984. *Monthly Weather Review*, 115, 51–74. https://doi.org/10.1175/1520-0493(1987)115,0051:TRBLSC.2.0.CO;2

Asher, W. E., Jessup, A. T., Branch, R., & Clark, D. (2014). Observations of rain-induced near-surface salinity anomalies. *Journal of Geophysical Research, Oceans*, 119, 5483–5500. https://doi.org/10.1002/2014JC009954

Bell, G. D., Halpert, M., & L'Heureux, M. (2016). ENSO and the tropical Pacific [in "State of the climate in 2015"]. *Bulletin of the American Meteorological Society*, 97, S93–S98.

Bellenger, H., Drushka, K., Asher, W., Reverdin, G., Katsumata, M., & Watanabe, M. (2016). Extension of the prognostic model of sea surface temperature to rain-induced cool and fresh lenses. *Journal of Geophysical Research, Oceans*, 121. https://doi.org/10.1002/2016JC012429

Berg, W., L'Ecuyer, T., & Kummerow, C. (2006). Rainfall climate regimes: The relationship of TRMM rainfall biases to the environment. *Journal of Applied Meteorology and Climatology*, 45, 434–454. https://doi.org/10.1175/JAM2331.1

Boutin, J., Chao, Y., Asher, W., Delcroix, T., Drucker, R., Drushka, K., … Ward, B. (2016). Satellite and *in situ* salinity: Understanding near-surface stratification and subfootprint variability. *Bulletin of the American Meteorological Society*, 97, 1391–1407. https://doi.org/10.1175/BAMS-D-15-00032.1

Boutin, J., Martin, N., Reverdin, G., Morisset, S., Yin, X., Centurioni, L., & Reul, N. (2014). Sea surface salinity under rain cells: SMOS satellite and *in situ* drifters observations. *Journal of Geophysical Research, Oceans*, 119, 5533–5545. https://doi.org/10.1002/2014JC010070

Boutin, J., Martin, N., Reverdin, G., Yin, X., & Gaillard, F. (2013). Sea surface freshening inferred from SMOS and Argo salinity: Impact of rain. *Ocean Science*, 9, 183–192. https://doi.org/10.5194/os-9-183-2013

Bowman, K. P. (2005). Comparison of TRMM precipitation retrievals with rain gauge data from ocean buoys. *Journal of Climate*, 18, 178–190. https://doi.org/10.1175/JCLI3259.1

Drushka, K., Asher, W. E., Ward, B., & Walesby, K. (2016). Understanding the formation and evolution of rain-formed fresh lenses at the ocean surface. *Journal of Geophysical Research, Oceans*, 121, 2673–2689. https://doi.org/10.1002/2015JC011527

ECMWF. (2004). *Early medium-range forecasts of tropical cyclones*. ECMWF Newsletter 102. Reading, England: ECMWF.

Fore, A. G., Yueh, S. H., Tang, W., Stiles, B. W., & Hayashi, A. K. (2016). Combined active/passive retrievals of ocean vector wind and sea surface salinity with SMAP. *IEEE Transactions on Geoscience and Remote Sensing*, 54, 7396–7404. https://doi.org/10.1109/TGRS.2016.2601486

Gaillard, F., Autret, E., Thierry, V., Galaup, P., Coatanoan, C., & Loubrieu, T. (2009). Quality control of large Argo datasets. *Journal of Atmospheric and Oceanic Technology*, 26, 337–351. https://doi.org/10.1175/2008jtecho552.1

Hasson, A., Delcroix, T., Boutin, J., Dussin, R., & Ballabrera-Poy, J. (2014). Analyzing the 2010–2011 La Niña signature in the tropical Pacific sea surface salinity using *in situ* data, SMOS observations, and a numerical simulation. *Journal of Geophysical Research, Oceans*, 119, 3855–3867. https://doi.org/10.1002/2013JC009388

Henocq, C., Boutin, J., Reverdin, G., Petitcolin, F., Arnault, S., & Lattes, P. (2010). Vertical variability of near-surface salinity in the tropics: Consequences for L-band radiometer calibration and validation. *Journal of Atmospheric and Oceanic Technology*, 27, 192–209. https://doi.org/10.1175/2009JTECHO670.1

Hilburn, K. A., & Wentz, F. J. (2008). Intercalibrated passive microwave rain products from the unified microwave ocean retrieval algorithm (UMORA). *Journal of Applied Meteorology and Climatology*, 47, 778–794. https://doi.org/10.1175/2007JAMC1635.1

Ho, D. T., Asher, W. E., Schlosser, P., Bliven, L., & Gordon, E. (2000). On the mechanisms of rain-induced air–water gas transfer. *Journal of Geophysical Research*, 105, 24045–24057. https://doi.org/10.1029/1999JC000280

Hong, Y., Gochis, D., Cheng, J., Hsu, K., & Sorooshian, S. (2007). Evaluation of PERSIANN-CCS rainfall measurement using the NAME event rain gauge network. *Journal of Hydrometeorology*, 8, 469–482. https://doi.org/10.1175/JHM574.1

Hou, A. Y., Kakar, R. K., Neeck, S., Azarbarzin, A. A., Kummerow, C. D., Kojima, M., … Iguchi, T. (2014). The global precipitation measurement (GPM) mission. *Bulletin of the American Meteorological Society*, 95, 701–722. https://doi.org/10.1175/BAMS-D-13-00164.1

Houze, R. A., Jr. (2004). Mesoscale convective systems. *Reviews of Geophysics*, 42, RG4003. https://doi.org/10.1029/2004RG000150

Huffman, G. J. (2015a). *GPM L3 IMERG final half hourly 0.1 degree x 0.1 degree precipitation V03*. Greenbelt, MD: Goddard Earth Sciences Data and Information Services Center (GES DISC). https://doi.org/10.5067/GPM/IMERG/HH/3B

Huffman, G. J. (2015b). *GPM L3 IMERG late half hourly 0.1 degree x 0.1 degree precipitation V03*. Greenbelt, MD: Goddard Earth Sciences Data and Information Services Center (GES DISC) Retrieved from https://disc.gsfc.nasa.gov/datacollection/GPM_3IMERGHHL_V03.html

Huffman, G. J., Bolvin, D. T., & Nelkin, E. J. (2015). *Integrated Multi-satellitE retrievals for GPM (IMERG)*, Technical Documentation. Greenbelt, MD: NASA Goddard Space Flight Center.

Joyce, R. J., Janowiak, J. E., Arkin, P. A., & Xie, P. (2004). CMORPH: A method that produces global precipitation estimates from passive microwave and infrared data at 8 km, hourly resolution. *Journal of Climate*, 5, 487–503. https://doi.org/10.1175/1525-7541(2004)005,0487:CAMTPG.2.0.CO;2

Kerr, Y. H., Waldteufel, P., Wigneron, J. P., Delwart, S., Cabot, F., Boutin, J., … Mecklenburg, S. (2010). The SMOS mission: New tool for monitoring key elements of the global water cycle. *Proceedings of the IEEE*, 98, 666–687. https://doi.org/10.1109/jproc.2010.2043032

Kidd, C., & Huffman, G. (2011). Global precipitation measurement. *Meteorological Applications*, 18, 334–353. https://doi.org/10.1002/met.284

Kidd, C., Panegrossi, G., & Ringerud, S., & Stocker, E. (2017, 23–28 April). *Inter-comparison of the EUMETSAT H-SAF and NASA PPS precipitation products over Western Europe*. Proceedings of the 19th EGU General Assembly, EGU2017. Vienna, Austria. p. 7506.

Kummerow, C. D., Olson, W. S., & Giglio, L. (1996). A simplified scheme for obtaining precipitation and vertical hydrometeor profiles from passive microwave sensors. *IEEE Transactions on Geoscience and Remote Sensing*, 34, 1213–1232.

Portabella, M., Stoffelen, A., Lin, W., Turiel, A., Verhoef, A., Verspeek, J., & Ballabrera-Poy, J. (2012). Rain effects on ASCAT retrieved winds: Toward an improved quality control. *IEEE Transactions on Geoscience and Remote Sensing*, 50, 2495–2506. https://doi.org/10.1109/tgrs.2012.2185933

Reverdin, G., Morisset, S., Boutin, J., & Martin, N. (2012). Rain-induced variability of near sea-surface T and S from drifter data. *Journal of Geophysical Research*, 117, C02032. https://doi.org/10.1029/2011JC007549

Santos-Garcia, A., Jacob, M. M., Jones, W. L., Asher, W. E., Hejazin, Y., Ebrahimi, H., & Rabolli, M. (2014). Investigation of rain effects on Aquarius sea surface salinity measurements. *Journal of Geophysical Research, Oceans*, 119, 7605–7624. https://doi.org/10.1002/2014JC010137

Schlussel, P., Soloviev, A. V., & Emery, W. J. (1997). Cool and freshwater skin of the ocean during rainfall. *Boundary-Layer Meteorology*, 82, 437–472. https://doi.org/10.1023/A:1000225700380

Serra, Y. L., & McPhaden, M. J. (2003). Multiple time- and space-scale comparisons of ATLAS rain gauge measurements with TRMM satellite precipitation measurements. *Journal of Applied Meteorology*, 42, 1045–1059. https://doi.org/10.1175/1520-0450(2003)042<1045:MTASCO>2.0.CO;2

Soloviev, A., Lukas, R., & Matsuura, H. (2002). Sharp frontal interfaces in the near-surface layer of the tropical ocean. *Journal of Marine Systems*, 37, 47–68. https://doi.org/10.1016/S0924-7963(02)00195-1

Sorooshian, S., Hsu, K. L., Gao, X., Gupta, H. V., Imam, B., & Braithwaite, D. (2000). Evaluation of PERSIANN system satellite-based estimates of tropical rainfall. *Bulletin of the American Meteorological Society*, 81, 2035–2046. https://doi.org/10.1175/1520-0477(2000)081,2035:EOPSSE.2.3.CO;2

SPURS-2 Planning Group. (2015). From salty to fresh—Salinity Processes in the Upper-ocean Regional Study-2 (SPURS-2): Diagnosing the physics of a rainfall-dominated salinity minimum. *Oceanography*, 28, 150–159. https://doi.org/10.5670/oceanog.2015.15

Stephens, G. L., & Kummerow, C. D. (2007). The remote sensing of clouds and precipitation from space: A review. *Journal of the Atmospheric Sciences*, 64, 3742–3765. https://doi.org/10.1175/2006JAS2375.1

Vila, D., Ferraro, R., & Joyce, R. (2007). Evaluation and improvement of AMSU precipitation retrievals. *Journal of Geophysical Research*, 112, D20119. https://doi.org/10.1029/2007JD008617

Walesby, K., Vialard, J., Minnett, P. J., Callaghan, A. H., & Ward, B. (2015). Observations indicative of rain-induced double diffusion in the ocean surface boundary layer. *Geophysical Research Letters*, 42, 3963–3972. https://doi.org/10.1002/2015GL063506

Waliser, D. E., & Gautier, C. (1993). A satellite-derived climatology of the ITCZ. *Journal of Climate*, 6, 2162–2174.

Wijesekera, H. W., Paulson, C. A., & Huyer, A. (1999). The effect of rainfall on the surface layer during a westerly wind burst in the western equatorial Pacific. *Journal of Physical Oceanography*, 29, 612–632. https://doi.org/10.1175/1520-0485(1999)029<0612:TEOROT>2.0.CO;2

Yin, X. B., Boutin, J., Martin, N., Spurgeon, P., Vergely, J.-L., & Gaillard, F. (2014). Errors in SMOS sea surface salinity and their dependency on *a priori* wind speed. *Remote Sensing of Environment*, 146, 159–171. https://doi.org/10.1016/j.rse.2013.09.008

Zabolotskikh, E., & Chapron, B. (2015). Validation of the new algorithm for rain rate retrieval from AMSR2 data using TMI rain rate product. *Advances in Meteorology*, 2015, 492603. https://doi.org/10.1155/2015/492603

Zappa, C. J., Ho, D. T., McGillis, W. R., Banner, M. L., Dacey, J. W. H., Bliven, L. F., … Nystuen, J. (2009). Rain-induced turbulence and air–sea gas transfer. *Journal of Geophysical Research*, 114, C07009. https://doi.org/10.1029/2008JC005008

How to cite this article: Supply A, Boutin J, Vergely J-L, *et al*. Precipitation Estimates from SMOS Sea-Surface Salinity. *Q J R Meteorol Soc* 2018;144 (Suppl. 1):103–119. https://doi.org/10.1002/qj.3110